



# Magnetic Fields Recorded by Chondrules Formed in Nebular Shocks

Chuhong Mai<sup>1</sup>, Steven J. Desch<sup>1</sup>, Aaron C. Boley<sup>2</sup>, and Benjamin P. Weiss<sup>3</sup>

<sup>1</sup> School of Earth and Space Exploration, Arizona State University, Tempe, AZ 85287-1404, USA; [chuhong.mai@asu.edu](mailto:chuhong.mai@asu.edu)

<sup>2</sup> Department of Physics and Astronomy, University of British Columbia, 6224 Agricultural Road, Vancouver BC V6T 1Z1, Canada

<sup>3</sup> Department of Earth, Atmospheric, and Planetary Sciences, Massachusetts Institute of Technology, 77 Massachusetts Avenue, Cambridge, MA 02139, USA

Received 2017 October 11; revised 2018 March 12; accepted 2018 March 13; published 2018 April 19

## Abstract

Recent laboratory efforts have constrained the remanent magnetizations of chondrules and the magnetic field strengths to which the chondrules were exposed as they cooled below their Curie points. An outstanding question is whether the inferred paleofields represent the background magnetic field of the solar nebula or were unique to the chondrule-forming environment. We investigate the amplification of the magnetic field above background values for two proposed chondrule formation mechanisms, large-scale nebular shocks and planetary bow shocks. Behind large-scale shocks, the magnetic field parallel to the shock front is amplified by factors of  $\sim 10$ – $30$ , regardless of the magnetic diffusivity. Therefore, chondrules melted in these shocks probably recorded an amplified magnetic field. Behind planetary bow shocks, the field amplification is sensitive to the magnetic diffusivity. We compute the gas properties behind a bow shock around a 3000 km radius planetary embryo, with and without atmospheres, using hydrodynamics models. We calculate the ionization state of the hot, shocked gas, including thermionic emission from dust, thermal ionization of gas-phase potassium atoms, and the magnetic diffusivity due to Ohmic dissipation and ambipolar diffusion. We find that the diffusivity is sufficiently large that magnetic fields have already relaxed to background values in the shock downstream where chondrules acquire magnetizations, and that these locations are sufficiently far from the planetary embryos that chondrules should not have recorded a significant putative dynamo field generated on these bodies. We conclude that, if melted in planetary bow shocks, chondrules probably recorded the background nebular field.

**Key words:** magnetic fields – meteorites, meteors, meteoroids – protoplanetary disks – shock waves

## 1. Introduction

The evolution of protoplanetary disks is strongly affected by magnetic fields. In weakly magnetized disks—those with background magnetic fields less than about 1 G—the magnetorotational instability (MRI) can operate and lead to turbulence and angular momentum transport (Balbus & Hawley 1998; Turner & Sano 2008). In strongly magnetized disks—those with background magnetic fields stronger than about 1 G—magnetocentrifugal winds can be launched, removing angular momentum from the disk and allowing accretion (Blandford & Payne 1982; Konigl & Pudritz 2000; Wardle 2007). Whether one mechanism or the other operates depends on the background magnetic field as well as the magnetic diffusivity. Regarding the MRI, it is widely appreciated that large zones of protoplanetary disks are probably insufficiently ionized for the gas to couple to the magnetic field (Gammie 1996; Jin 1996; Bai & Stone 2013; Turner et al. 2014). The exact coupling of the disk to the magnetic field depends on the diffusivities associated with not just Ohmic dissipation, but also ambipolar diffusion and the Hall effect (e.g., Desch 2004), and therefore is sensitive to the strength and orientation of the magnetic field. The rate of MRI-driven accretion is suppressed in weakly magnetized disks and is predicted to be about one order of magnitude lower than observed values. Regarding magnetocentrifugal winds, field strengths between about 1 and 30 G are required to explain observed stellar accretion rates (Wardle 2007), and the rate at which mass is launched in the wind depends on the rate of ambipolar diffusion. Depending on the field strength and other factors, magnetic fields are potentially the dominant driver of protoplanetary disk evolution. Yet very little data exist on the magnetic field strength in extant protoplanetary disks or the

solar nebula. While observations of the polarization of millimeter emission are beginning to reveal the geometry of magnetic fields in protoplanetary disks (Stephens et al. 2014; Li et al. 2016), the strength of the magnetic field is only poorly constrained to be  $>0.01$  G (Crutcher 2012; Li et al. 2016).

Only recently have new laboratory analyses of meteorites begun to open a window into the magnetic field of the solar nebula. Highly sensitive measurements (Fu et al. 2014, 2015) have revealed the remanent magnetization of chondrules, igneous inclusions in meteorites that formed in the solar nebula. Chondrules are millimeter- to submillimeter-sized igneous droplets found in abundance in chondritic meteorites. They are primarily composed of ferromagnesian silicates (olivines and pyroxenes), but often contain other minerals such as Fe-sulfide (troilite) or metallic FeNi (kamacite). Textural and chemical evidence strongly indicates that chondrules were “flash-heated” within minutes from temperatures below 650 K to temperatures above the liquidus, becoming free-floating molten objects in the presence of solar nebula gas; over the course of hours, they cooled and crystallized (Lofgren & Lanier 1990; Rubin 1999; Connolly & Desch 2004; Lauretta et al. 2006; Desch et al. 2012). The heating events that melted precursors and formed most chondrules took place in the protoplanetary disk, about 1.5–4.0 Myr after the formation of calcium-rich, aluminum-rich inclusions (CAIs), the first solids to form in the solar nebula (Kurahashi et al. 2008). As chondrules crystallized and cooled from the Curie points of their constituent ferromagnetic minerals within them (e.g., the Curie point of kamacite is 1038 K) to ambient space temperatures, the strength of the magnetic field in the chondrule-forming region would be continuously recorded as thermoremanent magnetization by

those minerals. About 10% of chondrules found in the Semarkona LL3.0 chondrites have “dusty olivines,” olivine phenocrysts containing kamacite inclusions capable of retaining magnetizations (Fu et al. 2014, 2015). Magnetizations of different directions have been recorded in the Semarkona chondrules, indicating that chondrules were exposed to magnetic fields before accretion into the Semarkona parent body (Fu et al. 2014, 2015). These studies show that the strength of the magnetic field chondrules were exposed to on average was  $\approx 0.54 \pm 0.21$  G. In contrast, the magnetizations of chondrules in the CR chondrite LAP02342 may indicate a weaker magnetic field  $< 0.15$  G (Fu et al. 2015). These measurements improved on earlier attempts that did not test for random orientations of the magnetizations that would indicate a pre-accretionary paleofield (Fu et al. 2014).

Although the magnetic field strengths in the chondrule-forming region are beginning to be constrained by meteoritic analyses, it is not yet clear how these relate to the background magnetic field of the solar nebula. The relationship between the background field and the paleofield in the chondrule-forming region depends on the exact chondrule formation mechanism. Several theories of chondrule formation have been proposed. A successful model of chondrule formation must be tested against experimental and other constraints regarding the timing, frequency, and physical conditions of chondrule formation, as well as the thermal histories experienced by chondrules (see Desch et al. 2012 for a review). Some of the well-developed models include ejection of molten chondrules by impact between asteroids (e.g., Urey & Craig 1953; Asphaug et al. 2011; Johnson et al. 2015); melting of chondrules in flares near the early Sun, as in the “X-wind” model (Shu et al. 1996, 1997, 2001); melting by lightning in the solar nebula (Morfill et al. 1993; Pilipp et al. 1998; Desch & Cuzzi 2000); melting of chondrules by large-scale shocks in the solar nebula, such as those produced by gravitational instabilities (e.g., Wood 1984, 1996; Desch & Connolly 2002; Boley & Durisen 2008; Morris & Desch 2010); or small-scale shocks in the solar nebula, such as bow shocks produced by planetesimals (e.g., Hood 1998; Ciesla et al. 2004; Hood et al. 2009) or planetary embryos (Morris et al. 2012; Boley et al. 2013; Mann et al. 2016) on eccentric orbits. The magnetic field in the chondrule-forming region may reflect the background value of the solar nebula, or not, depending on how chondrules actually formed, and depending on the geometry of the magnetic field and the rate of magnetic diffusivity in the chondrule-forming region.

For example, in the impact model, chondrules rapidly leave the vicinity of a parent body and can be expected to record the background field of the nebula. Chondrules formed according to the “X wind” model would be melted very near ( $\sim 0.1$  au) from the early Sun, in a unique environment near the magnetospheric radius, where the magnetic field geometry drives a magnetocentrifugal outflow. Though Shu et al. (1996) predicted fields of 0.4–8 G for the location where X-wind produced chondrules cooled, chondrules melted here could be exposed to fields of 10 G or more (Bai & Stone 2013), and these paleofields would not represent the overall background field of the protoplanetary disk. If chondrules were melted by nebular lightning, it is unclear what paleofields they would record. While fulgurites (soils melted by lightning strikes) record magnetic fields associated with the lightning strike itself ( $> 1$  T), through the process known as lightning-induced

remanent magnetization (e.g., Sakai et al. 1998; Sakai & Yonezawa 2002; Salminen et al. 2013), it is not at all clear that the magnetic fields associated with solar nebula lightning currents can be maintained for the hours it took chondrules to cool. As such, chondrules melted by lightning probably would record the background magnetic field, but that is uncertain. Finally, in the case of chondrule formation by solar nebula shocks, chondrule precursors are melted as they pass through the shock front and they cool and crystallize in the post-shock region. As we show in Section 2, in the post-shock region of a large-scale, 1D shock, the magnetic field is amplified above the background magnetic field of the nebula by a factor  $\chi$  that varies from  $\chi \sim 1$  for shocks propagating parallel to the magnetic field, to  $\chi \sim \mathcal{M}^2 \sim 30$  (where  $\mathcal{M}$  is the Mach number) for shocks propagating across field lines. These results are independent of the magnetic diffusivity. In contrast, in a small-scale, effectively 2D shock, magnetic diffusivity can play an important role. If magnetic diffusivity is low, the post-shock magnetic field can remain amplified by a factor  $\chi$  as in a 1D shock; but if magnetic diffusivity is high, the magnetic flux amplified behind the shock can diffuse laterally, returning the magnetic field in the post-shock region to the background value.

In this paper, we examine in greater detail the post-shock evolution of the magnetic field behind planetary embryo bow shocks. The paleofields recorded by chondrules melted by mechanisms other than shocks are simple to interpret: chondrules melted by impacts or lightning presumably record the background field of the nebula, and chondrules melted by the X wind mechanism presumably record the magnetic field close to the early Sun. The paleofields recorded by chondrules melted by large-scale 1D shocks are analytically simple; this is considered in Section 2. The last example, of chondrules melted in small-scale planetary embryo bow shocks, is more complicated and is the focus of the present paper. In Section 3.1, we discuss the temperature, pressure, and density of gas behind the shock of an atmosphere-free planetary embryo, for which we draw on the results of modeling using the hydrodynamics code Bozxy Hydro (Boley et al. 2013). Because the magnetic diffusivity is important in this case, we calculate in Section 3.2 the ionization of gas in the post-shock region using the formalism in Desch & Turner (2015), including not only thermal ionization of gas-phase potassium, but also thermionic emission of electrons and ions from hot dust grains. In Section 3.3, we use these computed ionization fractions to calculate the magnetic diffusivities associated with Ohmic dissipation and ambipolar diffusion. We compare the calculated magnetic diffusivities with the simulated trajectories of chondrules through the bow shock in Section 3.4 and show that the majority of chondrules could not record an amplified paleofield upon cooling down from the Curie point.

We also show that the chondrules cool sufficiently far away from the embryo such that if its metallic core was generating a dynamo, this would impart only a relatively weak magnetization on the chondrules relative to the nebular field. In Section 3.5, we perform similar calculations to a protoplanet with a thick atmosphere. We show that most chondrules cool down far downstream and avoid the region where the magnetic field can stay amplified and also avoid any embryo dynamo fields. We conclude in Section 4 that if chondrules are melted by planetary embryo bow shocks, then they record the

background magnetic field of the solar nebula. We also discuss the implications for the protoplanetary disk evolution.

## 2. Large-scale (1D) Nebula Shocks

Before considering the more complicated case of 2D planetary embryo bow shock, we first consider the evolution of the magnetic field behind a large-scale 1D shock. Large-scale shock waves are consistent with most of the experimental constraints on chondrule formation and are a leading model for chondrule formation (Desch et al. 2012). Potentially, they can be generated by accretion shocks (Wood 1984; Ruzmaikina & Ip 1994), infalling clumps (Tanaka et al. 1998), or tidal effects from passing stars (Larson 2002). Large-scale shocks at the disk midplane, which are most consistent with the constraints on chondrule formation, can be generated readily by global gravitational instabilities (Wood 1996; Boss & Durisen 2005). Such shocks have lateral extent  $\sim 1$  au, comparable to the size of the disk, much greater than the effective thickness of the shock,  $\sim 10^5$  km (Desch & Connolly 2002). They are effectively 1D. Due to the simplified geometry, the evolution of the magnetic field can be calculated analytically.

In the flux-freezing limit, the behavior of the magnetic field is especially straightforward to calculate. The gas motion is described by the mass continuity equation:

$$\frac{\partial \rho}{\partial t} + \nabla \cdot (\rho \mathbf{v}) = 0, \quad (1)$$

or, using the advective derivative,

$$\frac{d\rho}{dt} = -\rho(\nabla \cdot \mathbf{v}). \quad (2)$$

In addition to this equation is the magnetic field evolution equation in the flux-freezing approximation:

$$\frac{\partial \mathbf{B}}{\partial t} - \nabla \times (\mathbf{v} \times \mathbf{B}) = 0. \quad (3)$$

Using  $\nabla \cdot \mathbf{B} = 0$  and rewriting using the advective derivative yields

$$\frac{d\mathbf{B}}{dt} = \mathbf{B} \cdot \nabla \mathbf{v} - \mathbf{B}(\nabla \cdot \mathbf{v}). \quad (4)$$

Combining, one finds

$$\frac{d}{dt} \left( \frac{\mathbf{B}}{\rho} \right) = \frac{1}{\rho} \mathbf{B} \cdot \nabla \mathbf{v}. \quad (5)$$

For the case in which the magnetic field is perpendicular to the velocity gradients, the right-hand side vanishes, and one finds that the magnetic field does not change direction, and its strength is proportional to the density,  $\rho$ . For the case where the gradients and the flow direction are along the magnetic field, it is straightforward to show that the magnetic field is constant and uniform.

These equations are even simpler in the context of a steady state, 1D shock. We consider a 1D shock in which  $\mathbf{v}$  is along the  $x$  direction,  $\mathbf{B}$  is along the  $z$  direction, and all variations are along the  $x$  direction. In that case, assuming a steady-state solution, we must have

$$\frac{\partial}{\partial x} (vB) = 0, \quad (6)$$

leading to the “jump condition” across the shock front:

$$v_{\text{pre}} B_{\text{pre}} = v_{\text{post}} B_{\text{post}}. \quad (7)$$

Note that velocities are defined relative to the frame of the shock. The equation of mass conservation yields a very similar formula relating the density before and after the shock:

$$\rho_{\text{pre}} v_{\text{pre}} = \rho_{\text{post}} v_{\text{post}}, \quad (8)$$

so we can write

$$\frac{B_{\text{post}}}{B_{\text{pre}}} = \frac{v_{\text{pre}}}{v_{\text{post}}} = \frac{\rho_{\text{post}}}{\rho_{\text{pre}}} \equiv \chi. \quad (9)$$

For an adiabatic gas with adiabatic index  $\gamma$ ,

$$\chi = \frac{(\gamma + 1)\mathcal{M}^2}{(\gamma - 1)\mathcal{M}^2 + 2}, \quad (10)$$

where

$$\mathcal{M}^2 = \frac{\bar{m} V_s^2}{\gamma k T_{\text{pre}}} \quad (11)$$

is the Mach number squared,  $V_s$  being the shock speed (e.g., Shore 1992). In the strong-shock limit ( $\mathcal{M}^2 \gg 1$ ),  $\chi \approx (\gamma + 1)/(\gamma - 1) \approx 6$  typically. But if the gas can radiate, then  $\chi$  can reach higher values: in an isothermal shock, the compression factor is  $\chi \approx 2\gamma/[(\gamma + 1)\mathcal{M}^2]$  and is technically unlimited. The calculations of Desch & Connolly (2002) find  $\chi \sim 11$  for the shocks most likely to produce chondrules, at the post-shock location where chondrules reach the Curie point. We consider  $\chi \approx 10$ –30 to represent the typical compression of the magnetic field.

Because solar nebula gas is only partially ionized, the assumption of flux freezing is not always justified, and we must include nonideal magnetohydrodynamic effects in the magnetic field evolution equation, as follows:

$$\frac{\partial \mathbf{B}}{\partial t} - \nabla \times (\mathbf{v} \times \mathbf{B}) = -\nabla \times (\mathcal{D} \nabla \times \mathbf{B}), \quad (12)$$

where  $\mathcal{D} = (c^2/4\pi)\eta_{\perp}$  is the coefficient of magnetic diffusion (and  $\eta_{\perp}$  the resistivity) associated with currents perpendicular to the magnetic field (Parks 1991). This diffusion coefficient includes the effects of Ohmic dissipation and ambipolar diffusion and depends in a complicated way on the ionization fraction, the density and temperature, and the local magnetic field strength. The Hall diffusion term can be neglected here as we are mainly considering a poloidal magnetic field in the background. We revisit the calculation of  $\mathcal{D}$  in Section 3.3. For now, we assume that  $\mathcal{D}$  is uniform in the preshock region.

If we assume steady state and the same 1D geometry as above, we must have

$$\frac{\partial}{\partial x} \left( vB - \mathcal{D} \frac{\partial B}{\partial x} \right) = 0. \quad (13)$$

It is straightforward to show that the solution to this equation is

$$B_{\text{pre}}(x) = B_0 + B_0(\chi - 1)e^{+x/L} \quad (14)$$

$$B_{\text{post}} = \chi B_0, \quad (15)$$

where  $B_0$  is the background magnetic field strength in the solar nebula,  $L = \mathcal{D}/V_s$  is a characteristic diffusion lengthscale, and the preshock region is defined by  $x < 0$ . The magnetic field is



compressed by the shock by a factor of  $\chi$ . Because magnetic flux cannot diffuse in the lateral direction, it remains compressed in the post-shock region. Magnetic flux does diffuse into the preshock region, but the diffusion of this flux is exactly canceled by the advection of magnetic flux into the shock by the supersonic gas. The surprising result is that chondrules melted by large-scale shocks will record the amplified magnetic field, not the background magnetic field, regardless of the magnetic diffusivity (unless the shock velocities are exactly along the magnetic field lines).

### 3. Planetary Embryo Bow Shocks

Large-scale nebular shocks are a mechanism consistent with almost all experimental and other constraints on chondrule formation. The bow shocks around planetary embryos are also largely consistent with the constraints (Morris et al. 2012; Boley et al. 2013; Mann et al. 2016). The basic idea behind the model is that planetary embryos  $>2500$  km in radius apparently existed in the solar nebula (Mars had largely formed by 1.8 Myr: Dauphas & Pourmand 2011). If any of these embryos were scattered or perturbed onto eccentric orbits ( $e > 0.25$  or so), then they would move supersonically, at speeds  $\sim 8$  km s $^{-1}$ , with respect to the gas (Morris et al. 2012). They would therefore drive a bow shock in front of them, and chondrule precursors passing through this shock front would be flash-heated and melted in ways consistent with constraints. Chondrule precursors first are heated as the shock front approaches, by infrared radiation emitted from the already-heated chondrules behind the shock front. Then the chondrules receive an intense pulse of frictional heating as they pass through the shock front and move supersonically with respect to the gas. After the aerodynamic stopping time (about 1 minute), the chondrules no longer have any relative velocity with respect to the gas. But they are still heated by thermal exchange with the hot, shocked gas, as well as by infrared radiation emitted by other chondrules. Eventually, the planetary body moves on, the system cools, and the melted precursors cool and crystallize, forming chondrules.

The planetary embryo bow shock model is inspired by and resembles earlier models of chondrule formation in planetesimal bow shocks (Hood 1998; Ciesla et al. 2004; Hood et al. 2005, 2009). The main difference is that planetary embryos are  $\sim 2500$  km in radius, as opposed to tens to hundreds of kilometers in radius. But the larger scale makes qualitative differences. For one thing, only larger planetary bodies could be perturbed into highly eccentric orbits as needed for bow shock formation (Hood & Weidenschilling 2012). For another, the planetary embryo bow shock model does not suffer from deficiencies of planetesimal bow shock models. The most severe of these is that any chondrules created by planetesimal bow shocks will be immediately accreted onto the body. For planetary embryos, the larger scale yields a larger stand-off distance between the shock front and the planetary surface, and only for embryos does the stand-off distance exceed the aerodynamic stopping distance. It is also the case that, as first pointed out by Ciesla et al. (2004), peak temperatures in planetesimal bow shocks ( $<1000$  km) are too low and cooling rates are too rapid to match the thermal histories of chondrules. In fact, the cooling rates in these small-scale shocks are about an order of magnitude faster than the already high cooling rates in planetary embryo bow shock models.

In this section, we calculate the rates of magnetic diffusion behind a planetary embryo bow shock. We construct a model for the gas density and temperature using the output of bow shock models similar to those in Boley et al. (2013). We then calculate the ionization state using the prescriptions of Desch & Turner (2015). We convert these ionizations into rates of magnetic diffusion, and then we compare the implied diffusion timescales to the dynamical timescales throughout the post-shock region. We show that in the regions in which chondrules will cool below their Curie points, the rates of magnetic diffusion are sufficiently high that the magnetic field strength should relax to the preshock, background value.

#### 3.1. 3D Bow Shock Model

We first establish the background conditions using output obtained in the 2D/3D planetary embryo bow shock models (i.e., we use a 2D grid that captures 3D effects using cylindrical cells with corresponding updates on the hydrodynamics). These simulations use output from the 3D, second-order accurate radiation hydrodynamics code called Boxzy Hydro (Boley et al. 2013). The Cartesian grid includes 960 cells along the  $x$  axis and 400 cells along the other directions, with a resolution of 37.4 km. The planetary embryo, with radius 3000 km and mass  $3.4 \times 10^{26}$  g, is held stationary in these simulations, while gas is allowed to flow along the  $x$  axis, entering the computational domain with a uniform density  $10^{-9}$  g cm $^{-3}$ , temperature 300 K, and velocity  $V_s = 7$  km s $^{-1}$ . The gas is composed of 73 wt% H $_2$  and 25 wt% He, with heavier elements comprising 2% of the mass, yielding a mean molecular weight 2.33 amu. This code adopts an equation of state that includes the rotational and vibrational states of H $_2$ , as well as H $_2$  dissociation and recombination. In the particular run employed here, the ability to radiate is turned off, so that the gas behaves adiabatically. This is an optimistic scenario because gas tends to cool faster if radiating. For the particular science explored here, this assumption simplifies the simulation while leaving the nature of the problem unchanged. The code uses particle-in-cell methods for particle integration to keep track of dynamical feedback from solids on the gas. To simulate the trajectories of chondrule precursors passing through the bow shock, we inject  $10^6$  super-particles with random coordinates into the simulation domain, together with the wind flowing along the  $x$  axis. The solid-to-gas ratio is kept to be  $\sim 0.004$ , which is consistent with the average chondrule mass fraction ( $\sim 0.04$ ) and chondrule concentration factor ( $\sim 10$ ) for chondrule-forming regions in previous studies (Morris et al. 2012; Boley et al. 2013). Forty tracer particles with evenly increasing impact parameters up to 6000 km are selected from these super-particles. Their positions and corresponding physical properties (temperature, density, etc.) are regularly recorded during the simulation. The code is evolved for  $\sim 10^6$  s until a quasi-steady state is achieved. Major outputs include pressure, temperature, gas density, and velocity distribution. Figure 1 shows the representative temperature and gas density around the modeled planetary embryo.

#### 3.2. Ionization States

The degree to which gas couples dynamically to magnetic fields is determined by the magnetic diffusion rates, which in turn depend on the degree of ionization, among other factors. The rate of ionization of gas in disk midplanes is remarkably low, as energetic particles (Galactic cosmic rays, solar

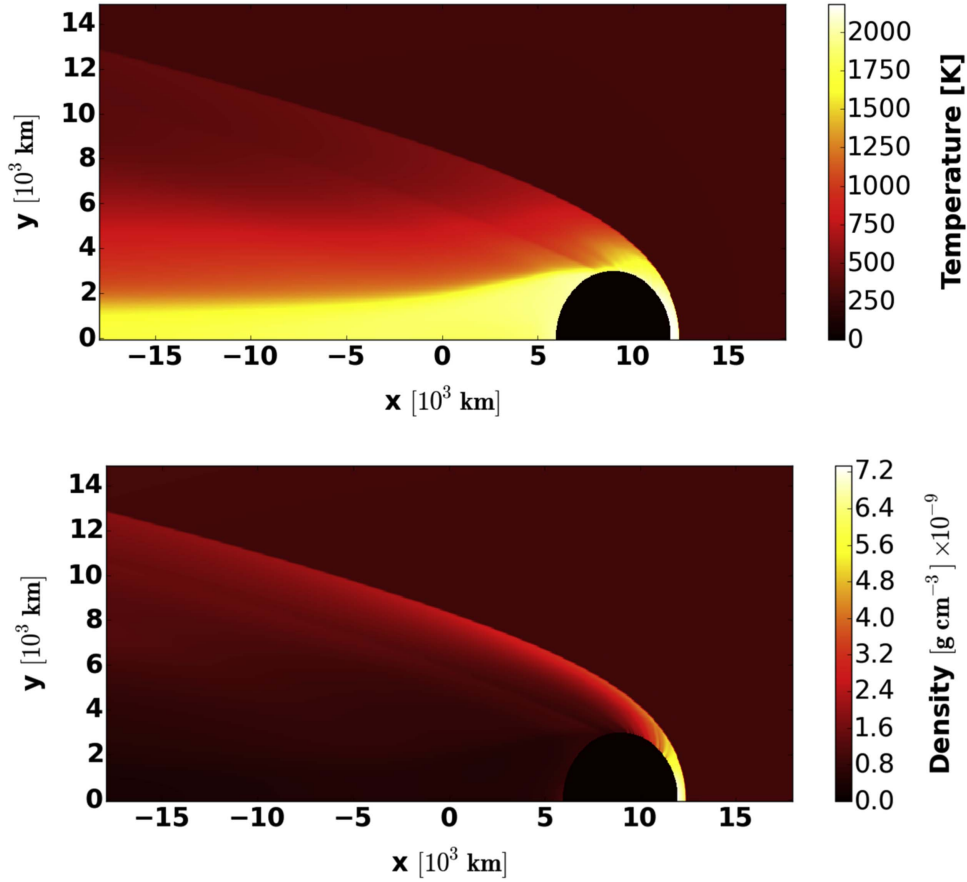
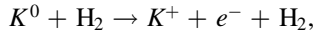
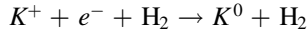


**Figure 1.** Representative gas temperature (top) and density (bottom) in the planetary bow shock region. The embryo is drawn in black.

energetic particles, and X-rays and UV photons from the star) are shielded by the disk gas. Essentially, the only source of ionization in cold gas is from radioactive decay, e.g., of  $^{40}\text{K}$ ,  $^{238}\text{U}$ ,  $^{235}\text{U}$ , and  $^{232}\text{Th}$ , at a rate  $\zeta \sim 10^{-22} \text{ s}^{-1}$  (Umebayashi & Nakano 2009) per  $\text{H}_2$  molecule, and of short-lived radionuclide  $^{26}\text{Al}$ ,  $\zeta \sim 10^{-18} \text{ s}^{-1}$  (Umebayashi & Nakano 1981). The ionization rate increases considerably with temperature as the gas heats above about 700 K, however, due to thermionic emission from hot solids, and at even higher temperatures from collisional ionization of gas-phase alkali atoms (Desch & Turner 2015). Traditionally, only the latter effect has been considered in disks, assuming that the rates of collisional ionization of alkalis,



is in detailed balance with the rate of gas-phase recombinations,



(where  $K$  is the alkali element that contributes most strongly to ionization). If these were in balance, then one could apply the equilibrium Saha equation to calculate the ionization fraction as a function of temperature:

$$\frac{n_{K^+}}{n_{K^0}} = \frac{g_+}{g_0} \frac{2}{n_e} \left( \frac{2\pi m_e kT}{h^2} \right)^{3/2} \exp\left(-\frac{\text{IP}}{kT}\right), \quad (16)$$

where  $n_{K^+}$ ,  $n_{K^0}$ , and  $n_e$  are densities of potassium ions and atoms, and electrons,  $g_+ = 1$  and  $g_0 = 2$  are statistical weights of  $K^+$  and  $K^0$ ,  $m_e$  is the electron mass,  $k$  is Boltzmann's constant,  $h$  is Planck's constant, and  $\text{IP} = 4.34 \text{ eV}$  is the first

ionization potential energy of potassium. In fact, as demonstrated by Desch & Turner (2015), the recombination of alkali ions is primarily on dust surfaces, as ions and electrons that adsorb onto the same grain can quantum tunnel over the grain surface until they recombine (and most likely leave as a neutral atom). Sticking of electrons or ions on grain surfaces is in fact in detailed balance with emission of electrons or ions from grain surfaces by the process of thermionic emission, at a rate given by Richardson's law:

$$j(T) = \lambda_R \frac{4\pi m_e (kT)^2}{h^3} \exp\left(-\frac{W}{kT}\right), \quad (17)$$

where  $j(T)$  is temperature-dependent rate of electron emission per grain surface area,  $\lambda_R$  is a material-dependent dimensionless constant,  $W$  is the work function of the solid, and other constants have their usual meanings. Because the work functions of astrophysical solids typically are  $\approx 5 \text{ eV}$ , the ionization due to thermionic emission approximates that of thermal ionization, especially above about 1500 K, but differs significantly at lower temperatures (Desch & Turner 2015). The exponential factor present in both the Saha equation and Richardson's law highlights the sensitivity of the ionization to temperature.

We take the temperature from the output of the planetary bow shock models; as seen in Figure 1, the temperature ranges from 300 K to over 2000 K in the bow shock region. We adopt the chemical network built by Desch & Turner (2015), which includes thermal ionization, gas-phase recombination,

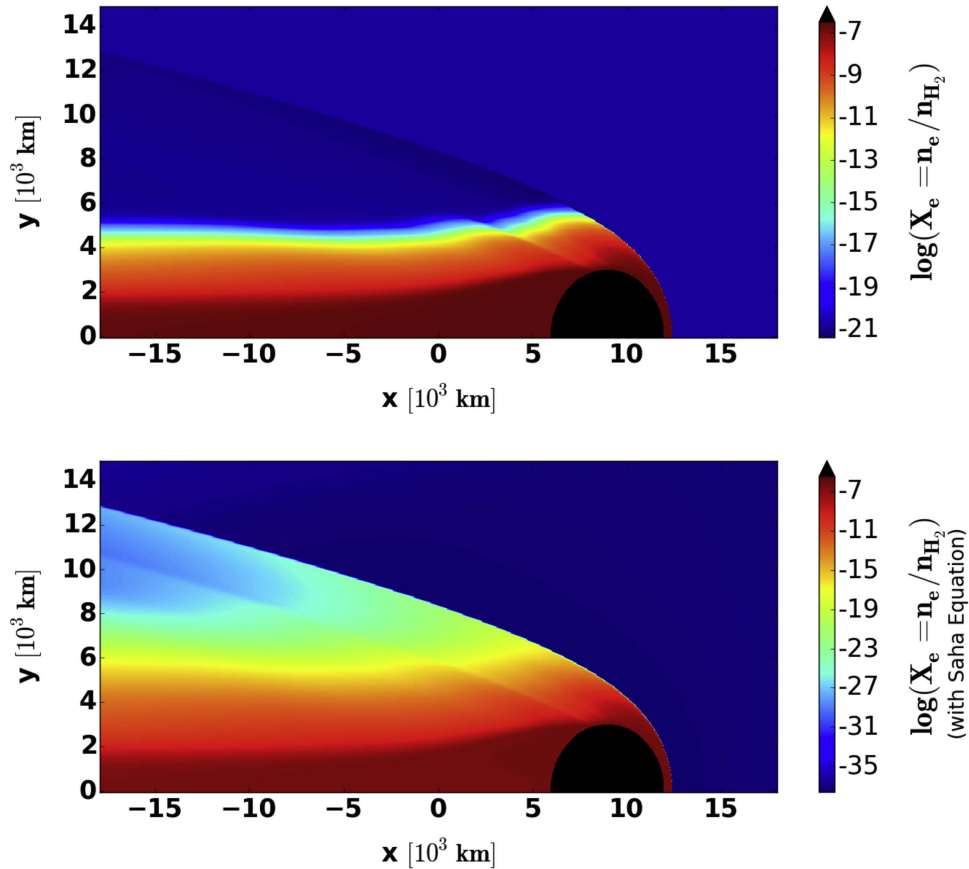


**Figure 2.** Electron fraction in the post-shock gas behind the planetary embryo bow shock. The post-shock region has a relatively high ionization fraction, especially directly behind the planetary body (drawn as a black circle). The upper panel considers thermionic emission from hot dust grains while the lower panel shows the results using the Saha equation, as a comparison. See the text for a discussion.

adsorption following collisions onto dust grains, and thermionic emission of electrons and ions ( $K^+$ ) and neutral  $K^0$  atoms from grain surfaces. This formalism returns the steady-state densities of free electrons ( $e^-$ ), neutral and ionized gas-phase atoms ( $Mg^+$ ), neutral and ionized gas-phase alkali atoms ( $K^0$ ,  $K^+$ ), and grain-adsorbed alkali atoms ( $K^{0*}$ ), as well as the densities of neutral and charged grains ( $g^+$ ,  $g^0$ ,  $g^-$ ), as a function of density ( $\rho$ ), temperature ( $T$ ), abundances, and grain mass fraction, and background nonthermal ionization rate  $\zeta$ . The steady-state assumption is justified at the higher temperatures of interest: for  $T > 1500$  K, ionization equilibrium is achieved in less than 2–3 minutes, and in less than an hour for  $T > 1200$  K (Desch & Turner 2015, Figure 5). Rather than run the code at every location, we ran it separately to generate a lookup table that returns the above densities as a function of temperature and hydrogen number density ( $n_H = \rho / (2.8 m_H)$ , to account for He). We assume a solids-to-gas mass ratio of 0.004, a grain radius  $1 \mu m$  and internal density  $3 g cm^{-3}$ , and a particle work function  $W = 5.0 eV$  appropriate for ferromagnesian silicates. We find that for the conditions typical of the high-temperature regions behind the bow shock, the dominant ionization mechanism is emission from dust surfaces, and the dominant recombination mechanism is adsorption onto dust surfaces, so the ionization state is relatively insensitive to the exact details of particle size or solids-to-gas mass ratio. Figure 2 upper panel shows the electron fraction  $n_e/n_H$  as a function of location behind the shock. Densities of other charged particles follow similar spatial distributions. As a

comparison, we also used the Saha equation (Equation (16)) to find the electron fraction (Figure 2 lower panel). The results deviate from the lookup table at low temperatures, as the Saha equation predicts a much smaller ionization fraction in those regions. At temperatures around  $1500 \sim 2000$  K, the ionization state around the planetary bow shock is adequately described by the Saha equation.

### 3.3. Magnetic Diffusion

For the case in which magnetic fields are perfectly coupled to the fluid (the flux-freezing approximation), the main determinant of how well magnetic fields couple to the gas is the degree of ionization, but other factors matter as well, especially magnetic field strength and geometry, and density and temperature. We consider Ohmic dissipation and ambipolar diffusion as diffusion mechanisms: the Hall effect can sometimes dominate, but under almost all conditions in protoplanetary disks, either Ohmic dissipation or ambipolar diffusion dominates (Desch & Turner 2015). The diffusion rate depends on the magnetic field geometry: if the electric currents are parallel to the magnetic field, the diffusion coefficient  $\mathcal{D}_{\parallel}$  is proportional to the parallel resistivity,  $\eta_{\parallel}$ , which is due entirely to Ohmic dissipation:  $\eta_{\parallel} = \eta_{OD}$ . If the electric currents are perpendicular to the magnetic field, the diffusion coefficient  $\mathcal{D}_{\perp}$  is proportional to the perpendicular resistivity,  $\eta_{\perp}$ , which is the sum of contributions from Ohmic dissipation and ambipolar diffusion:  $\eta_{\perp} = \eta_{OD} + \eta_{AD}$  (e.g.,

Desch & Mouschovias 2001). We do not calculate the magnetic field geometry, so we cannot quantify the relative contributions of Ohmic dissipation and ambipolar diffusion to the uncoupling of the magnetic field from the gas; therefore, we consider the rate of magnetic diffusion to be bracketed by  $\mathcal{D}_{\parallel}$  and  $\mathcal{D}_{\perp}$ .

The magnetic diffusion coefficients are related to the resistivities as  $\mathcal{D}_{\parallel} = (c^2/4\pi)\eta_{\parallel}$  and  $\mathcal{D}_{\perp} = (c^2/4\pi)\eta_{\perp}$ , where the resistivities are related to the conductivities,  $\sigma$ , as

$$\eta_{\parallel} = \eta_{\text{OD}} = \frac{1}{\sigma_{\parallel}} \quad (18)$$

and

$$\eta_{\perp} = \eta_{\text{OD}} + \eta_{\text{AD}} = \frac{\sigma_{\perp}}{\sigma_{\perp}^2 + \sigma_{\text{H}}^2}, \quad (19)$$

where

$$\sigma_{\parallel} = \sum_s \sigma_s \quad (20)$$

$$\sigma_{\perp} = \sum_s \frac{\sigma_s}{1 + (\omega_s \tau_{sn})^2} \quad (21)$$

$$\sigma_{\text{H}} = -\sum_s \frac{\sigma_s \omega_s \tau_{sn}}{1 + (\omega_s \tau_{sn})^2}, \quad (22)$$

where  $\sigma_{\parallel}$  is the direct conductivity,  $\sigma_{\perp}$  the Pedersen conductivity, and  $\sigma_{\text{H}}$  the Hall conductivity. Here  $\sigma_s = n_s q_s^2 \tau_{sn} / m_s$  is the conductivity of each species  $s$ , where  $n_s$ ,  $q_s$ , and  $m_s$  are the number density, charge, and mass of each charged species,  $\omega_s = q_s B / m_s c$  is the gyrofrequency of species  $s$  around magnetic field lines, and  $\tau_{sn}$  is the momentum exchange timescale for charged species  $s$  in a sea of neutral particles, formulas of which are taken from Pinto & Galli (2008). The conductivities sum over the charged species  $e^-$ ,  $\text{Mg}^+$  and  $\text{K}^+$ .

For the parallel conductivity, it is straightforward to show that the conductivity from electrons dominates, in which case the diffusion coefficient reduces to a much simpler form:

$$\mathcal{D}_{\parallel} = \mathcal{D}_{\text{OD}} = \frac{9060}{x_e} \left( \frac{T}{1500 \text{ K}} \right)^{1/2} \text{ cm}^2 \text{ s}^{-1}, \quad (23)$$

where  $x_e = n_e / n_{\text{H}_2}$  (Blaes & Balbus 1994). Unlike  $\mathcal{D}_{\parallel}$ ,  $\mathcal{D}_{\perp} = \mathcal{D}_{\text{OD}} + \mathcal{D}_{\text{AD}}$  depends on the magnetic field strength. In fact, to first order,  $\mathcal{D}_{\text{AD}} \propto B^2$ . In the calculations that follow, we assume  $B = 0.5 \text{ G}$ , consistent with the paleofield measured by Fu et al. (2014); larger magnetic fields would lead to greater rates of magnetic diffusion. We note that  $0.5 \text{ G}$  is a relatively weak magnetic field, resulting in a plasma beta  $\beta = 8\pi P / B^2 \sim 10^3$  for  $P \sim 10^{-5} \text{ bar}$ . The magnetic diffusion coefficients are depicted in Figure 3, which shows  $\mathcal{D}_{\parallel}$  and  $\mathcal{D}_{\perp}$  behind the bow shock. Also depicted is the rough boundary where  $\mathcal{D} < 3 \times 10^{13} \text{ cm}^2 \text{ s}^{-1}$ .

### 3.4. Results

The magnetic diffusion coefficients provide a rough idea of whether the magnetic field will remain amplified past the bow shock, or whether it will relax to the background field. The magnetic diffusion timescale, the time it takes for magnetic flux

to diffuse laterally into the unshocked region, is

$$t_{\text{diff}} \sim \frac{L^2}{\mathcal{D}}, \quad (24)$$

where  $\mathcal{D}$  pertains to either  $\mathcal{D}_{\parallel}$  or  $\mathcal{D}_{\perp}$ , and  $L \sim R_p \sim 3000 \text{ km}$  is a relevant lengthscale. For comparison, the dynamical timescale for gas to flow past the planetary body is

$$t_{\text{dyn}} \sim \frac{L}{V}, \quad (25)$$

where  $V$  is the post-shock velocity of gas and chondrules. If  $t_{\text{diff}} < t_{\text{dyn}}$ , then the magnetic field has time to relax to the background state by the time the chondrules reach the Curie point. That is, if  $\mathcal{D}$  exceeds a critical value  $\mathcal{D}_{\text{crit}} \sim LV$ , then chondrules will record a magnetic field relaxed to the background state. Using  $L \sim 3000 \text{ km}$  and  $V \sim 1 \text{ km s}^{-1}$  yields  $\mathcal{D}_{\text{crit}} \sim 3 \times 10^{13} \text{ cm}^2 \text{ s}^{-1}$ . To be more precise, the dynamical timescale is the time it takes chondrules to reach their Curie point, or drop in temperature by about 1000 K. The cooling rates of chondrules in planetary bow shocks are  $\approx 1000\text{--}2000 \text{ K hr}^{-1}$ , meaning that chondrules will reach their Curie points after traveling downstream for about  $t_{\text{dyn}} = 30\text{--}60$  minutes, for a distance of about 2400–4800 km. On the other hand, the distance magnetic flux must travel laterally is, as is apparent from Figure 3, less than 3000 km. On the whole, we judge  $\mathcal{D}_{\text{crit}} \sim 3 \times 10^{13} \text{ cm}^2 \text{ s}^{-1}$  to be an accurate threshold.

In Figure 3, the blue dashed lines mark the threshold  $\mathcal{D} = \mathcal{D}_{\text{crit}}$  for both  $\mathcal{D}_{\parallel}$  and  $\mathcal{D}_{\perp}$ . Therefore, in regions above the dashed lines, magnetic flux has sufficient time to diffuse laterally and relax to the background magnetic field strength. The fate of the magnetic field in the hot regions is less clear: it may or may not be amplified behind the shock, depending on the geometry. A behavior sometimes seen in the simulations of Boley et al. (2013) is that shocked gas sometimes cools and then heats up again because it enters the hot region behind the planetary embryo. If the gas cooled sufficiently for tens of minutes, magnetic flux may diffuse out of that gas, relaxing to the background field, before it becomes frozen in the gas again. A calculation of the magnetic field behind the planetary embryo is beyond the scope of this paper. What can be said with certainty is that in all other regions, where  $\mathcal{D} > \mathcal{D}_{\text{crit}}$ , the magnetic field almost certainly relaxed to the background field of the nebula.

All that remains is to show what region chondrules are in when they reach their Curie points and begin to record the local magnetic field. In Figure 3, we overlay the simulated trajectories of chondrules with the magnetic diffusivity maps. The trajectories are colored light orange where the chondrules are heated up to above 1038 K, the Curie point of kamacite. The points where the orange trajectories become white again in the post-shock region mark where chondrules cool down to their Curie points. It is quickly seen that under the action of Ohmic dissipation alone, most chondrules cool down at the edge of the low diffusivity region. Although it may seem tricky to judge whether the chondrules record an enhanced magnetic field or the background field, or a field strength in between at a first glance, we conclude that it is safe to state that most chondrules are magnetized beyond the critical diffusivity threshold line. For one, chondrules record the field during cooling from the Curie point continuously down to ambient space temperatures. Even though the locations of the kamacite



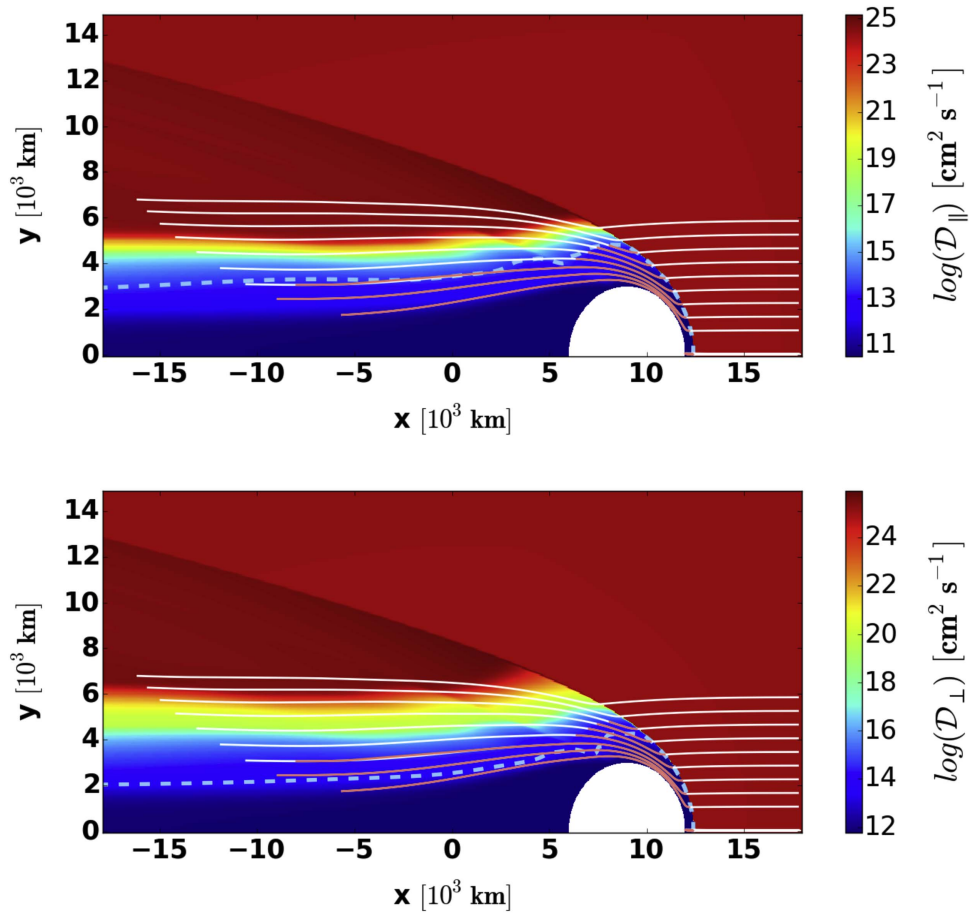


**Figure 3.** Magnetic diffusivity  $\mathcal{D}_{\parallel}$  (top) and  $\mathcal{D}_{\perp}$  (bottom) around the planetary embryo (drawn as white). The blue dashed line depicts the critical diffusivity threshold  $\mathcal{D} = 3 \times 10^{13} \text{ cm}^2 \text{ s}^{-1}$ . Above the dashed line, the magnetic field is considered highly diffusive. The white solid lines are the simulated trajectories of chondrules under adiabatic conditions, with the parts where chondrule precursors are hotter than 1038 K (the kamacite Curie point) colored as light orange. On the whole, the majority of chondrules cool down from the Curie point in regions beyond the critical threshold and record the background magnetic field. See discussions in the text.

Curie points overlap with where the critical diffusivity threshold line lies, the majority of chondrules would largely record a diffused magnetic field after passing this line, as they cool from the Curie temperature down to the ambient temperature. For another, due to the existence of the background magnetic field, ambipolar diffusion also plays a non-negligible role in diffusing the magnetic field. Under the combined action of Ohmic dissipation and ambipolar diffusion, it is clear that the vast majority of chondrules reach 1038 K beyond the critical diffusivity threshold in the highly diffusive region. Even at the relatively weak magnetic field strength of 0.5 G, ambipolar diffusion may significantly enhance the rate of magnetic flux diffusion. Note that in these simulations we have assumed that the chondrules are in thermal equilibrium with the surrounding gas. In reality, chondrules might experience effective radiative cooling and cool down at higher rates in the post-shock region. But even if the temperature difference between gas and chondrules is as large as 100 K, the results would not be changed much and the above discussions remain valid. Moreover, 1038 K is the highest Curie temperature of minerals found in chondrules, yet still not high enough for the gas to maintain an ionization fraction large enough to “freeze” the magnetic field. Lower Curie points, like those of taenite (<873 K), martensite magnetite (853 K), and pyrrhotite (600 K), would be reached further beyond the critical diffusivity threshold line.

Figure 4 is essentially the same as Figure 3’s top panel, except that the magnetic diffusivity  $\mathcal{D}_{\parallel}$  is derived from ionization fractions calculated using the Saha equation (Figure 2 lower panel). Due to the lack of thermionic emission from dust grains, the ionization levels in regions with temperatures around 1000 K are much lower. Therefore, the flux-freezing region shrinks and the critical diffusivity threshold line moves downward, compared to Figure 3 (top panel). Chondrules are supposed most likely to record a diffused background field in such a scenario.

To test the sensitivity of our results, we also performed bow shock simulations under different sets of initial parameters. By increasing the relative velocity of the planetary embryo to disk gas to  $10 \text{ km s}^{-1}$ , we produce a post-shock region with a larger high-temperature area. Both the critical diffusivity threshold lines and the locations of the Curie points of chondrules are correspondingly shifted further away from the planetary embryo. The conclusion that most chondrules would record a nebular magnetic field remains unchanged. We also altered the size of injecting chondrule precursors by one standard deviation from the original input ( $\sim 0.03 \text{ cm}$ ), assuming they follow a log-normal size distribution (Nelson & Rubin 2002). The different sizes of chondrules change the survival rates of the population, but not the bulk pattern of their trajectories, and therefore not the locations of their Curie points. Our previous conclusion still holds.



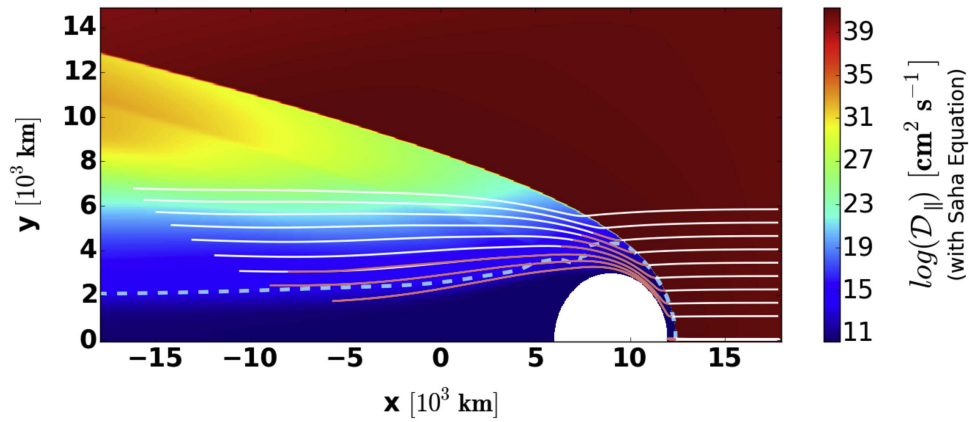


**Figure 4.** Magnetic diffusivity  $\mathcal{D}_{\parallel}$  around the planetary embryo calculated using the Saha equation (ignoring dust effects on ionization). Lines and symbols have the same meanings as those in Figure 3. See the text for discussions.

On the whole, it is safe to say that chondrules spend almost all of their time, and certainly the time after they reach their Curie temperatures, outside of the region where magnetic fields can be amplified. Chondrules melted in bow shocks should record the background field of the nebula.

We end this section by considering the implications of these calculations for the possibility that the chondrules might have recorded a magnetic field generated by the embryo. In particular, Recent paleomagnetic studies of achondrites have found that early planetary bodies likely generated dynamo magnetic fields with surface paleointensities of  $\sim 0.1$ – $1$  G (Fu et al. 2012; Bryson et al. 2015; Wang et al. 2017). Figures 3 and 4 show that the chondrules reach the kamacite Curie temperatures at a distance of  $\sim 1.5$  to  $>7$  planetary radii from the embryo’s center. If we assume that its dynamo field is dipolar, then scaling the paleointensities above shows that this would have occurred where the embryo’s dynamo field was somewhere between  $\sim 10^{-5}$  and  $0.3$  G. Even the latter maximum value is about a factor of  $\sim 2$  lower than that recorded by the Semarkona chondrules. Furthermore, a comparison of Figure 1 with Figures 3 and 4 shows that the chondrules reach their 750 K blocking temperatures at a distance of  $\sim 3$  planetary radii, at which point the dynamo field would be  $<0.04$  G, well below the  $0.54$  G paleointensity recorded by Semarkona. We conclude that total thermoremanent magnetization in chondrules formed from cooling from the Curie point to ambient space temperatures is unlikely to be the product of a planetesimal dynamo for paleointensities exceeding a few tens of mG.

### 3.5. The Influence of Planetary Protoatmospheres

As the planetary embryos are embedded in a gaseous protoplanetary disk, it is reasonable to believe that they are able to maintain protoatmospheres either through the accretion of nebula gas or outgassing from the planetary surface, or both. Particularly, Stokl et al. (2015) has pointed out that Earth-size protoplanets can hold up to thousands of bars of hydrogen-rich atmospheres when nebula gas is dissipated. Although some atmosphere loss mechanisms have been proposed for planets in their early life (e.g., ram-pressure stripping; ultraviolet and soft X-ray (XUV) radiation-driven escape; hydrodynamical effect from disk evaporation), the timescales of these escape processes are probably not small enough, compared to those of atmosphere

accretion and chondrule formation, to immediately remove the protoatmospheres. We believe the planetary embryo could possess an atmosphere in at least some portion of its time with a bow shock. We will revisit this topic later in the section.

The presence of an atmosphere could increase the shock size, modify the state variables, deflect chondrule trajectories, and thus probably provide a different scenario of magnetic diffusion and chondrule cooling in the bow shock. The amount of the atmosphere that the embryo retains is subject to planet mass, the accretion and stripping rates and the windspeed conditions at different orbital phases, and therefore should vary over time (Mann et al. 2016). Here we explore the two extreme cases, the atmosphere-free case discussed above in Sections 3.1–3.4 and the high-mass atmosphere case that will be discussed below, which should bracket any other possible cases where an atmosphere is present.

In the high-mass atmosphere case, we place an atmosphere mostly composed of  $\text{H}_2$  and He with polytropic structure, following a spherical symmetric density profile (Morris et al. 2012; Mann et al. 2016):

$$\rho(r) = \rho_0 \left[ 1 + H \left( \frac{1}{r} - \frac{1}{R_e} \right) \right]^{1/(\gamma-1)}, \quad (26)$$

where  $\rho_0$  is the surface gas density,  $r$  is the distance to the center of the planet,  $\gamma \sim 1.35$  is the adiabatic index, and  $R_e$  is the planet radius.  $H = \frac{GM(\gamma-1)}{\gamma K \rho_0^{\gamma-1}}$  functions similar to an atmosphere scale height,  $K$  is the polytropic constant. The atmosphere has a similar set up as in Mann et al. (2016), with a mass of about  $2.7 \times 10^{20}$  g, or 11 Martian atmospheres, and creates 14 mbar of surface pressure. The simulations are extended to include 800 cells along the  $x$  axis and 3200 cells along the  $y$  axis to better capture the physics. Figure 5 shows the representative temperature and gas density around the embryo with a thick atmosphere, as a comparison to Figure 1.

The existence of the atmosphere generates a cooler and denser boundary layer between the protoplanet and the post-shock gas flow. At this boundary, which reaches 13,000 km in radius behind the planetary embryo, vigorous turbulence, including Kelvin–Helmholtz (KH) instabilities, develop. As pointed out in Morris et al. (2012) and Ouellette et al. (2007), KH instabilities can strip away the atmosphere with an efficiency  $\sim 1\%$  (relative to the incident mass flux), translating

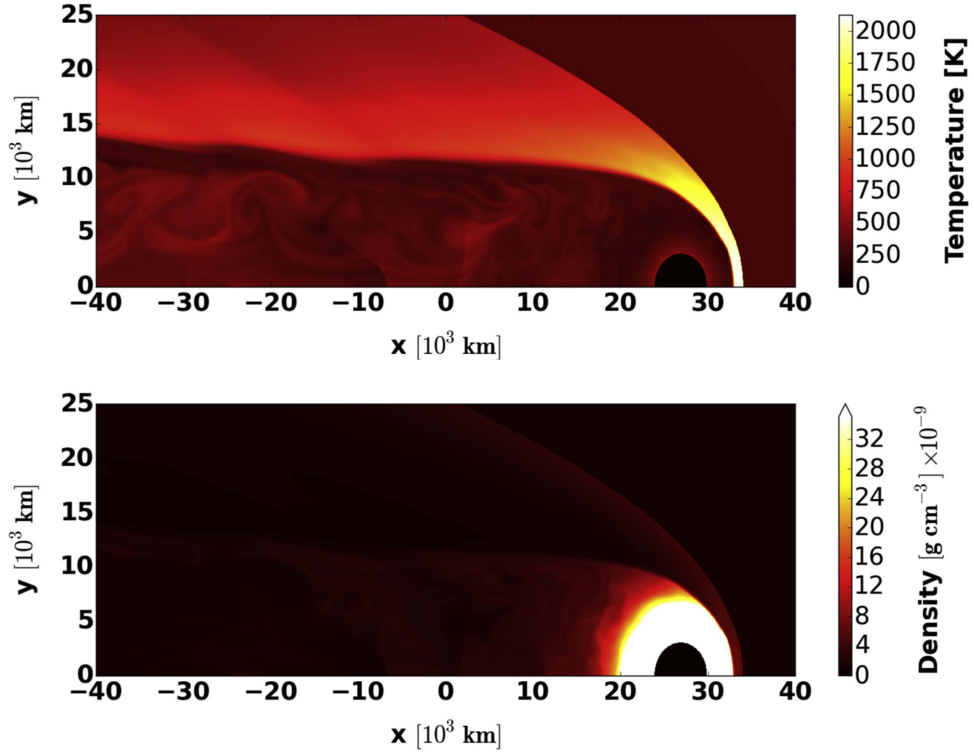


**Figure 5.** Snapshots of representative gas temperature (top) and density (bottom) in the bow shock region where a thick planetary proto-atmosphere is present. The planetary embryo is drawn in black.

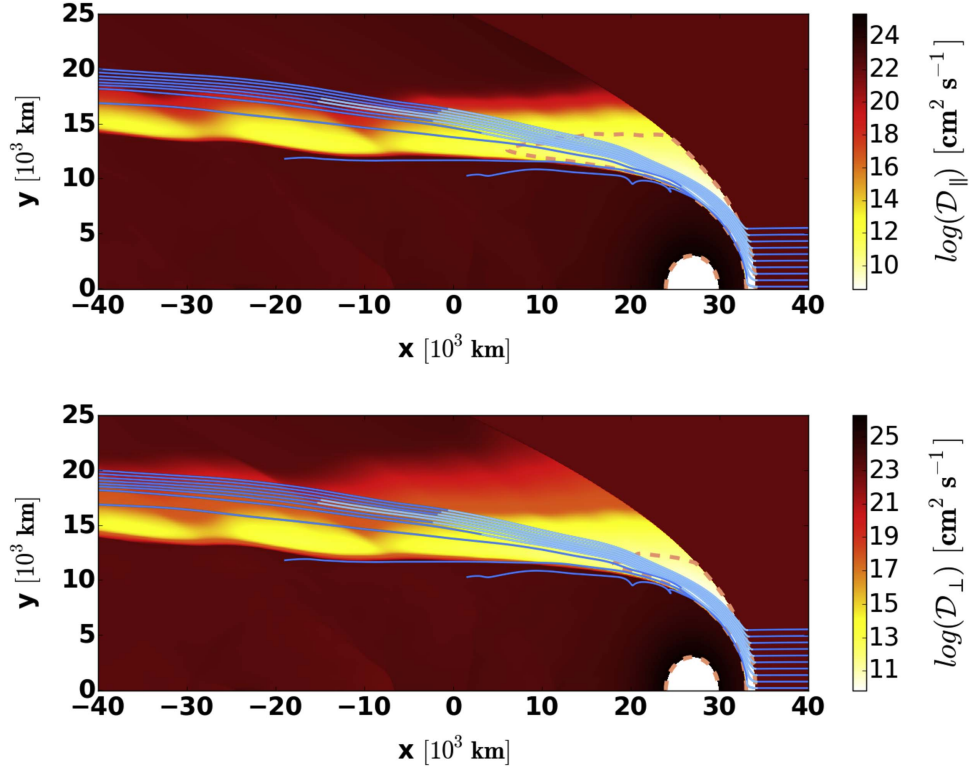


**Figure 6.** Magnetic diffusivity  $\mathcal{D}_{\parallel}$  (top) and  $\mathcal{D}_{\perp}$  (bottom) around the planetary embryo (drawn as white) with a thick atmosphere. Note that the color scheme is different from Figure 3 and adjusted for better visualization in the high-mass atmosphere case. The orange dashed line depicts the critical diffusivity threshold  $\mathcal{D} = 3 \times 10^{13} \text{ cm}^2 \text{ s}^{-1}$ . The amplified magnetic field in any region above the dashed line is quickly diffused to the background level. The blue solid lines are the simulated chondrule trajectories, with the parts where chondrule precursors are hotter than 1038 K colored as light blue. The vast majority of chondrules cool down far beyond the critical threshold and record the background magnetic field.

to an atmospheric mass-loss rate  $\sim 10^{12} \text{ g s}^{-1}$ . In their numerical simulations, Mann et al. (2016) measured a stripping rate of  $\sim 5 \times 10^{14} \text{ g s}^{-1}$ , which is considerably higher. Both rates are lower than the estimated Bondi accretion rate of a stationary atmosphere by one to three orders of magnitude. However, in reality, the atmosphere accretion rate is also affected by the relative motion between the protoplanet and the nebula gas and probably the bow shock structure itself. There are different phases of mass accretion and mass loss of the atmosphere depending on the details of the relative wind speeds as a function of embryo orbit. The impact of an eccentric orbit on atmosphere accretion is beyond the scope of this study, but remains a goal of our future work.

Following the same methodology layed out in Sections 3.2 and 3.3, we calculate the magnetic diffusivity  $\mathcal{D}_{\parallel}$  and  $\mathcal{D}_{\perp}$  for the high-mass atmosphere case (Figure 6). Unlike the atmosphere-free case, the thick atmosphere creates a large low-temperature high-diffusivity cylinder with a radius of 13,000 km behind the planet. The atmosphere also deflects the chondrule trajectories so drastically that very few chondrules that enter with low impact parameters make it into the high-diffusivity cylinder. Revolving trajectories are observed for these few chondrules under the influence of KH instability. It is clear that under either Ohmic dissipation alone or both Ohmic and ambipolar diffusion, the vast majority of chondrules cool down to their Curie points in the downstream of the post-shock region far away from the critical threshold contour line and are magnetized by the background nebula field. Again, considering the higher cooling rates of chondrules in reality, a temperature gap as large as 100 K between the gas and chondrules only alters the above results subtly. We conclude that the presence of an atmosphere significantly increases the chance that chondrules cool down in highly diffusive post-shock regions, and therefore record the background magnetic field.

We can also consider the possibility that chondrules were magnetized by a dynamo generated on the atmosphere-bearing embryo. Figure 6 shows that, in this case, the chondrules reach the kamacite Curie point at  $\sim 15$  planetary radii from the embryo. Again assuming a dipolar dynamo with surface intensity of 0.1–1 G, we see that the dynamo field at this distance is negligible ( $< 3 \times 10^{-4}$  G) and so cannot explain the Semarkona chondrule paleointensities.

#### 4. Discussion and Conclusions

In this article, we have determined the magnetic fields that would be recorded by chondrules melted by nebular shocks. In the case of large-scale shocks, such as those generated by gravitational instabilities in the protoplanetary disk, we find that magnetic fields parallel to the shock front are amplified by factors  $\chi \sim 10$ –30 regardless of the rate of magnetic diffusion, although magnetic fields normal to the shock front are not amplified. We also have considered the rate of magnetic diffusion in the gas behind a planetary embryo bow shock. We have used the output from the radiation hydrodynamics simulations to constrain the gas densities, and temperatures, and the trajectories of chondrules, in the post-shock region. We have calculated the ionization state of the post-shock gas using the formalism of Desch & Turner (2015), and computed the coefficients of magnetic diffusion due to Ohmic dissipation and ambipolar diffusion. In the case of an atmosphereless planetary embryo, we find that these coefficients typically exceed  $\mathcal{D}_{\text{crit}} \approx 3 \times 10^{13} \text{ cm}^2 \text{ s}^{-1}$  and will relax to the background

field, everywhere except the region near and behind the planetary body. If we consider only the effects of Ohmic dissipation, most chondrules have already cooled to their Curie points upon arriving at the critical diffusivity threshold. With the effects of ambipolar diffusion included, the majority cool down in regions where  $\mathcal{D} > \mathcal{D}_{\text{crit}}$ . Therefore, during their subsequent cooling to ambient temperatures, which is the time when they acquire remanent magnetization, they record the ambient (i.e., nonamplified) nebular field. On the whole, most chondrules are magnetized in the background magnetic field in the bow shocks produced by atmosphere-free protoplanets. In another extreme case where the planetary body possesses a thick atmosphere ( $2.7 \times 10^{20} \text{ g}$ ),  $\mathcal{D} < \mathcal{D}_{\text{crit}}$  except in a 13,000 km radius cylinder behind the planet and in the post-shock region far from the planet. Almost all the trajectories of chondrules lie outside of the highly diffusive cylinder. Yet the time and place they cool to their Curie points are far away enough in the downstream that they end up recording the background magnetic field anyway. As such, chondrules melted in planetary embryo bow shocks record magnetic fields in regions that have relaxed to the background magnetic field. We also show that the chondrules cool to ambient space temperatures sufficiently far from the embryos that they are unlikely to be substantially magnetized by possible dynamo fields generated in the embryos' metallic cores.

We can approximate the temperature below which  $\mathcal{D} > \mathcal{D}_{\text{crit}}$  and the rate of magnetic diffusion is rapid enough that the magnetic field relaxes to the background level. The temperature at the Curie point is 1038 K, and this is the relevant temperature at which to calculate the rate of magnetic diffusion. The ionization of the gas is dominated by thermionic emission, not collisional (thermal) ionizations, but we can approximate the behavior by using the Saha equation and assuming only Ohmic dissipation. In that case, the number density of  $K^+$  ions is given by the Saha equation and, assuming  $n_e = n_{K^+}$ , the number density of electrons is

$$\begin{aligned} x_e = \frac{n_e}{n_{\text{H}_2}} &= \left( \frac{n_{\text{K}_0}/n_{\text{H}_2}}{n_{\text{H}_2}} \right)^{1/2} \cdot \left( \frac{2g_+}{g_0} \right)^{1/2} \\ &\cdot \left( \frac{2\pi m_e kT}{h^2} \right)^{3/4} \cdot \exp\left(-\frac{\text{IP}}{2kT}\right) \\ &= 0.65 \cdot \left( \frac{n_{\text{H}_2}}{10^{14} \text{ cm}^{-3}} \right)^{-1/2} \cdot \left( \frac{T}{1500 \text{ K}} \right)^{3/4} \\ &\cdot \exp\left(-\frac{16.782}{T/1500 \text{ K}}\right). \end{aligned} \quad (27)$$

Combined with Equation (23), and assuming  $n_{\text{K}_0}/n_{\text{H}_2} \approx 3 \times 10^{-7}$  (Lodders 2003), it is quickly seen that  $\mathcal{D}_{\text{OD}} = \mathcal{D}_{\text{crit}}$  at a temperature of about 1175 K. At  $T \approx 1100 \text{ K}$ , using the Saha equation,  $\mathcal{D}_{\text{OD}} \approx 1.3 \times 10^{14} \text{ cm}^2 \text{ s}^{-1}$ , and the timescale to magnetic flux to diffuse laterally about 2000 km is about 5 minutes, about the same length of time for chondrules to cool from 1175 to 1038 K (at a cooling rate of  $2000 \text{ K hr}^{-1}$ ). By considering the ionization fraction due to thermionic emission, and including the effects of ambipolar diffusion, very similar results are obtained.

Fu et al. (2014) inferred paleofields of 0.54 G from chondrules in the L3.0 Semarkona chondrite. If these chondrules were melted by large-scale solar nebula shocks, then they would have recorded magnetic fields an order of magnitude greater than the background

magnetic field, implying background fields  $\sim 0.02\text{--}0.05$  G. However, gravitational instabilities that might drive large-scale shocks require a high surface density that is most likely early in the evolution of the protoplanetary disk, whereas chondrules in ordinary chondrites apparently formed at a protoplanetary disk age  $\approx 1.5\text{--}3$  Myr (Villeneuve et al. 2009). We view it as more likely that the chondrules in Semarkona were melted by passage through bow shocks in advance of planetary embryos on eccentric orbits (potentially due to resonant interactions with a recently formed massive Jupiter). In that case, the background magnetic field of the solar nebula is likely to be close to the paleofield recorded by the chondrules,  $\approx 0.5$  G.

A background magnetic field of the solar nebula disk  $\approx 0.5$  G compares well with theoretical estimates of the maximum fossil magnetic field in the region where chondrites formed ( $\approx 2\text{--}3$  au). Nakano & Umebayashi (1986a, 1986b) estimated field strengths  $\sim 1$  G in a region of size  $\sim 4$  au. Desch & Mouschovias (2001) calculated field strengths  $\sim 0.1$  G over a region of size  $\sim 20$  au during prestellar collapse, the exact value depending on parameters such as grain size and cosmic-ray ionization rate. If grains coagulated to radii  $> 1\text{ }\mu\text{m}$  during collapse, the magnetic field in this region would be  $> 0.5$  G (see also Zhao et al. 2006). Grain growth to this size during the molecular cloud stage is predicted (Mouschovias & Ciolek 1999). Masson et al. (2016) likewise found that magnetic fields are not amplified above about 0.1 G within tens of astronomical units. Kunz & Mouschovias (2010) performed similar calculations and found field strengths  $\sim 0.2$  G over regions  $\sim 2$  au in radius. These calculations all predict magnetic fields during prestellar collapse of a few tenths of a Gauss within the region where chondrules and chondrites will subsequently form.

A background magnetic field of the solar nebula disk  $\approx 0.5$  G is also consistent with the magnetic field needed to transport angular momentum in protoplanetary disks. If angular momentum and mass are radially transported by the MRI, then the magnetic field strength relates to the mass accretion rate as

$$B > 0.3 \left( \frac{\dot{M}}{10^{-8} M_{\odot} \text{ yr}^{-1}} \right)^{1/2} \left( \frac{r}{2.5 \text{ au}} \right)^{-11/8} \text{ G} \quad (28)$$


(Fu et al. 2014). Conversely, if angular momentum is transported by a magnetocentrifugal disk wind, then the magnetic field strength is related to mass accretion rate as

$$B > 0.03 \left( \frac{\dot{M}}{10^{-8} M_{\odot} \text{ yr}^{-1}} \right)^{1/2} \left( \frac{r}{2.5 \text{ au}} \right)^{-5/4} \text{ G} \quad (29)$$

(Fu et al. 2014). We favor minimal amplification of the magnetic field during chondrule formation, meaning that the magnetic fields recorded by Semarkona chondrules were sufficient to transport mass by either the MRI or by disk winds.

We would like to thank the anonymous referee for a careful reading and constructive comments, as well as suggestions that helped us improve this paper greatly. We are grateful to the support from NASA Emerging Worlds (PI Benjamin Weiss, NNX15AH72G). ACB's contribution was supported by an NSERC Discovery grant, The University of British Columbia, the Canadian Foundation for Innovation, and the BC Knowledge Development Fund. B. Weiss thanks Thomas F. Peterson, Jr. for his generous support.

## ORCID iDs

Chuhong Mai  <https://orcid.org/0000-0002-9243-5065>  
 Steven J. Desch  <https://orcid.org/0000-0002-1571-0836>  
 Aaron C. Boley  <https://orcid.org/0000-0002-0574-4418>  
 Benjamin P. Weiss  <https://orcid.org/0000-0003-3113-3415>

## References

- Asphaug, E., Jutzi, M., & Movshovitz, N. 2011, *LPICo*, **1608**, 1647  
 Bai, X.-N., & Stone, J. M. 2013, *ApJ*, **769**, 76  
 Balbus, S. A., & Hawley, J. F. 1998, *RvMP*, **70**, 1  
 Blaes, O. M., & Balbus, S. A. 1994, *ApJ*, **421**, 163  
 Blandford, R. D., & Payne, D. G. 1982, *MNRAS*, **199**, 883  
 Boley, A. C., & Durisen, R. H. 2008, *ApJ*, **685**, 1193  
 Boley, A. C., Morris, M. A., & Desch, S. J. 2013, *ApJ*, **776**, 101  
 Boss, A. P., & Durisen, R. H. 2005, *ApJ*, **621**, 137  
 Bryson, J. F. J., Nichols, C. I. O., Herrero-Albillos, J., et al. 2015, *Natur*, **517**, 472  
 Ciesla, F. J., Hood, L. L., & Weidenschilling, S. J. 2004, *M&PS*, **39**, 1809  
 Connolly, H. C., & Desch, S. J. 2004, *ChEG*, **64**, 95  
 Crutcher, R. M. 2012, *ARA&A*, **50**, 29  
 Dauphas, N., & Pourmand, A. 2011, *Natur*, **473**, 489  
 Desch, S. J. 2004, *ApJ*, **608**, 509  
 Desch, S. J., & Connolly, H. C. 2002, *M&PS*, **37**, 183  
 Desch, S. J., & Cuzzi, J. N. 2000, *Icar*, **143**, 87  
 Desch, S. J., Morris, M. A., Connolly, H. C., & Boss, A. P. 2010, *ApJ*, **725**, 692  
 Desch, S. J., Morris, M. A., Connolly, H. C., & Boss, A. P. 2012, *M&PS*, **47**, 1139  
 Desch, S. J., & Mouschovias, T. C. 2001, *ApJ*, **550**, 314  
 Desch, S. J., & Turner, N. J. 2015, *ApJ*, **811**, 156  
 Draine, B. T., & Sutin, B. 1987, *ApJ*, **320**, 803  
 Fu, R. R., Weiss, B. P., Lima, E. A., et al. 2014, *Sci*, **346**, 1089  
 Fu, R. R., Weiss, B. P., & Schrader, D. L. 2015, *LPICo*, **1832**, 1587  
 Fu, R. R., Weiss, B. P., Shuster, D. L., et al. 2012, *Sci*, **338**, 238  
 Gammie, C. F. 1996, *ApJ*, **457**, 355  
 Hood, L. L. 1998, *M&PS*, **33**, 97  
 Hood, L. L., Ciesla, F. J., Artemieva, N. A., Marzari, F., & Weidenschilling, S. J. 2009, *M&PS*, **44**, 327  
 Hood, L. L., Ciesla, F. J., & Weidenschilling, S. J. 2005, in *ASP Conf. Ser.* **341**, Chondrites and the Protoplanetary Disk (San Francisco, CA: ASP), 873  
 Hood, L. L., & Weidenschilling, S. J. 2012, *M&PS*, **47**, 1715  
 Ivanova, M. A., Kononkova, N. N., Franchi, I. A., et al. 2006, *LPSC*, **37**, 1100  
 Jin, L. 1996, *ApJ*, **457**, 798  
 Johnson, B. C., Minton, D. A., Melosh, H. J., & Zuber, M. T. 2015, *Natur*, **517**, 339  
 Konigl, A., & Pudritz, R. E. 2000, in *Protostars and Planets IV*, ed. V. Mannings (Tucson, AZ: Univ. Arizona Press), 759  
 Kunz, M. W., & Mouschovias, T. C. 2010, *MNRAS*, **408**, 322  
 Kurahashi, E., Kita, N. T., Nagahara, H., & Morishita, Y. 2008, *GeCoA*, **72**, 3865  
 Larson, R. B. 2002, *MNRAS*, **332**, 155  
 Lauretta, D. S., Nagahara, H., & Alexander, C. M. OD. 2006, *Meteorites and the Early Solar System II* (Tucson: Univ. Arizona Press), 431  
 Li, D., Pantin, E., Telesco, C. M., et al. 2016, *ApJ*, **832**, 18  
 Lodders, K. 2003, *ApJ*, **591**, 1220  
 Lofgren, G., & Lanier, A. B. 1990, *GeCoA*, **54**, 3537  
 Mann, C. R., Boley, A. C., & Morris, M. A. 2016, *ApJ*, **818**, 103  
 Masson, J., Chabrier, G., Hennebelle, P., Vaytet, N., & Commerçon, B. 2016, *A&A*, **587**, A32  
 Morfill, G., Spruit, H., & Levy, E. H. 1993, in *Protostars and Planets III* (Tucson, AZ: Univ. Arizona Press), 939  
 Morris, M. A., Boley, A. C., Desch, S. J., & Athanassiadou, T. 2012, *ApJ*, **752**, 27  
 Morris, M. A., & Desch, S. J. 2010, *ApJ*, **722**, 1474  
 Mouschovias, T. C., & Ciolek, G. E. 1999, in *The Origin of Stars and Planetary Systems* (Dordrecht: Kluwer), 305  
 Nakano, T., & Umebayashi, T. 1986a, *MNRAS*, **218**, 663  
 Nakano, T., & Umebayashi, T. 1986b, *MNRAS*, **221**, 319  
 Nelson, V. E., & Rubin, A. E. 2002, *M&PS*, **37**, 1361  
 Ouellette, N., Desch, S. J., & Hester, J. J. 2007, *ApJ*, **662**, 1268  
 Parks, G. K. 1991, in *Physics of Space Plasmas* (Redwood City: Addison-Wesley), 283  
 Pilipp, W., Hartquist, T. W., Morfill, G. E., & Levy, E. H. 1998, *A&A*, **331**, 121



- Pinto, C., & Galli, D. 2008, [A&A](#), **484**, 17
- Rubin, A. 1999, [GeCoA](#), **63**, 2281
- Ruzmaikina, T. M., & Ip, W.-H. 1994, [Icar](#), **112**, 430
- Sakai, H., Sunada, S., & Sakurano, H. 1998, [JEIEn](#), 123, 41
- Sakai, H., & Yonezawa, K. 2002, [PJAB](#), 78, 1
- Salminen, J., Pesonen, L. J., Lahti, K., & Kannus, K. 2013, [GeoJ](#), 195, 117
- Sanders, I. S. 1996, in *Chondrules and the Protoplanetary Disk* (Cambridge: Cambridge Univ. Press), 327
- Sanders, I. S., & Taylor, G. J. 2005, in *Chondrites and the Protoplanetary Disk*, Vol. 341 (San Francisco, CA: ASP), 915
- Shore, S. N. 1992, *An Introduction to Astrophysical Hydrodynamics* (San Diego, CA: Academic)
- Shu, F. H., Shang, H., Glassgold, A. E., & Lee, T. 1997, [Sci](#), **277**, 1475
- Shu, F. H., Shang, H., Gounelle, M., Glassgold, A. E., & Lee, T. 2001, [ApJ](#), **548**, 1029
- Shu, F. H., Shang, H., & Lee, T. 1996, [Sci](#), **271**, 1545
- Stephens, I. W., Looney, L. W., Kwon, W., et al. 2014, [Natur](#), **514**, 597
- Stokl, A., Dorfi, E., & Lammer, H. 2015, [A&A](#), **576**, A87
- Tanaka, K. K., Tanaka, H., Nakazawa, K., & Nakagawa, Y. 1998, [Icar](#), **134**, 137
- Turner, N. J., Fromang, S., Gammie, C., et al. 2014, in *Protostars and Planets VI*, ed. H. Beuther et al. (Vol. 914; Tucson: Univ. Arizona Press), 411
- Turner, N. J., & Sano, T. 2008, [ApJL](#), **679**, L131
- Umebayashi, T., & Nakano, T. 1981, [PASJ](#), **33**, 617
- Umebayashi, T., & Nakano, T. 2009, [ApJ](#), **690**, 69
- Urey, H. C. 1967, [Icar](#), **7**, 350
- Urey, H. C., & Craig, H. 1953, [GeCoA](#), **4**, 36
- Villeneuve, J., Chaussidon, M., & Libourel, G. 2009, [Sci](#), **325**, 985
- Wang, H., Weiss, B. P., Bai, X.-N., et al. 2017, [Sci](#), **355**, 623
- Wardle, M. 2007, [Ap&SS](#), **311**, 35
- Wood, J. A. 1984, *Metic*, **19**, 339
- Wood, J. A. 1996, [M&PS](#), **31**, 641
- Zhao, B., Caselli, P., Li, Z.-Y., et al. 2006, [MNRAS](#), **460**, 2050